UC Irvine
UC Irvine Previously Published Works

Title
Reachable and Controllable Sets for Planetary Entry and Landing

Permalink
https://escholarship.org/uc/item/7tt8875n

Journal
Journal of Guidance Control and Dynamics, 33(3)

ISSN
0731-5090

Authors
Benito, Joel
Mease, Kenneth D

Publication Date
2010-05-01

DOI
10.2514/1.47577

Peer reviewed

eScholarship.org Powered by the California Digital Library
University of California

Reachable and Controllable Sets for Planetary Entry and Landing

Joel Benito* and Kenneth D. Mease†
University of California, Irvine, 92697-3975

Understanding the envelope of entry trajectories that a given planetary lander is capable of flying can be an important aid for mission analysis and design. We consider two characteristics of this envelope: (i) the set of states reachable from a given entry state, and (ii) the set of entry states controllable to a given final state. Precise definitions of these sets are given and methods for computing them are presented. To illustrate their use, the sets are employed to characterize the Mars entry of two vehicle configurations, a low lift-to-drag ratio (L/D) capsule and a mid L/D ellipsled. A role for the sets in evaluating entry guidance algorithms is described.

Nomenclature

CS	=	controllable set
CFP	=	controllable footprint
C_D	=	drag coefficient
C_L	=	lift coefficient
C_γ	=	component of the Coriolis acceleration in the flight path angle equation
C_ψ	=	component of the Coriolis acceleration in the heading angle equation
D	=	drag acceleration
F	=	set of feasible control-trajectory pairs
g	=	gravitational acceleration
h	=	altitude
h_s	=	atmospheric density scale height

* Graduate Student, Mechanical and Aerospace Engineering; jbenitom@uci.edu.
† Professor, Mechanical and Aerospace Engineering; kmease@uci.edu. Associate Fellow AIAA.

J	=	cost function
k_q	=	stagnation point convective heat rate constant
L	=	lift acceleration
m	=	vehicle mass
P	=	set of states that do not violate path constraints
$\bar{q}$	=	dynamic pressure
Q	=	stagnation point convective heat load
$\dot{Q}$	=	stagnation point convective heat rate
RS	=	reachable set
RFP	=	reachable footprint
r	=	distance from planet's center to the vehicle's center of mass
r_n	=	nose radius
S	=	reference surface
T	=	transition map
U	=	set of admissible control profiles
V	=	velocity
V_s	=	speed of sound
γ	=	flight path angle
Δ	=	set of allowable deployment states
θ	=	longitude
μ	=	planet's gravitational constant
Π	=	longitude and latitude extraction map
ρ	=	atmospheric density
ρ_0	=	sea-level atmospheric density
σ	=	bank angle
ϕ	=	latitude

ψ	=	heading angle
ω_p	=	planet's rotation rate
X	=	set of allowable states

Subscripts

0	=	initial
f	=	final
(θ,ϕ)	=	restricted to a particular value of the (θ,ϕ) pair

Superscripts

J	=	minimizes the cost function *J*

I. Introduction

FOR planetary landing mission analysis and design, it is beneficial to characterize the envelope of trajectories that a given lander is capable of flying. In particular, two characteristics of this envelope are the focus of our attention: (i) the set of states reachable from a given entry state, and (ii) the set of entry states controllable to a given final state. The objectives of this paper are to define the reachable set (RS) and the controllable set (CS), present methods for their computation, and illustrate the use of these sets via a detailed application to Mars entry for two vehicle configurations.

Reachable and controllable sets are established concepts in mathematical systems theory; see for example Ref. [1]. We adapt the standard definitions to accommodate the particular features of entry flight – the boundary conditions and the path and control constraints. The landing footprint, a more familiar concept in flight mechanics, can be derived from the reachable set. The landing footprint is a two-dimensional set, typically given in terms of longitude and latitude. See Ref. [2] for an early paper describing landing footprints, Ref. [3] for optimal landing footprints, and Ref. [4] for a fast suboptimal computational approach. The RS is a six-dimensional set of values of the translational state variables for the entry vehicle. Using spherical coordinates for position and velocity as we do, two of the position coordinates are longitude and latitude. The landing footprint is, in a sense, a projection of the RS onto the longitude-latitude plane. Keeping track of the full translational state for the points that can be reached by a lander is important when state variables in addition to longitude and latitude are of interest. For example, there may

be multiple points in the RS with the same longitude and latitude, and the one of most interest might be the one with the highest altitude.

The controllable set is a generalization of the entry corridor. The entry corridor is typically defined as the one-dimensional set of the allowable entry flight path angles [2]. The determination of the entry corridor is important for mission planning and design, and it is in the list of recommendations for the design of entry guidance systems in Ref. [5]. A study of the effect of lift on the entry corridor is presented in Ref. [6]. A two-dimensional version of the entry corridor, accounting for variations of the entry angle with the entry velocity, has also been defined (see an example in Ref. [7]). Since the main entry trajectory constraints (such as heat rate and structural loads) and delivery requirements (such as downrange and altitude) are functions of the longitudinal state variables (velocity, flight path angle and radius), the lateral state variables are commonly ignored for the definition of the entry corridor. The entry interface is typically defined at a fixed altitude, and hence a two-dimensional entry corridor provides the necessary information for the characterization of the entry problem. Missions that require flexibility on the entry state, large crossrange and/or high landing accuracy may require a more complete representation that includes the lateral state variables. The CS generalizes the entry corridor by including both the longitudinal and lateral state variables in a six-dimensional set. The inclusion of the lateral state variables provides a complete representation of the entry states from which a vehicle can reach a given landing site. The projection of the CS in the latitude-longitude plane is the controllable footprint (CFP).

Figs. 1 and 2 sketch the RS and CS and their corresponding footprints. The sets presented in Figs. 1 and 2 are simplified 3-dimensional versions of the more complex 6-dimensional general sets, but they illustrate the concept.

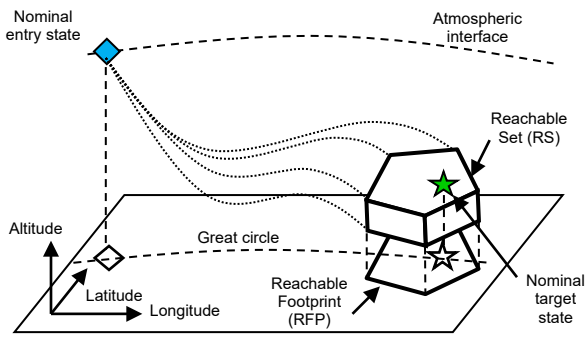

Fig. 1 Reachable set and reachable footprint

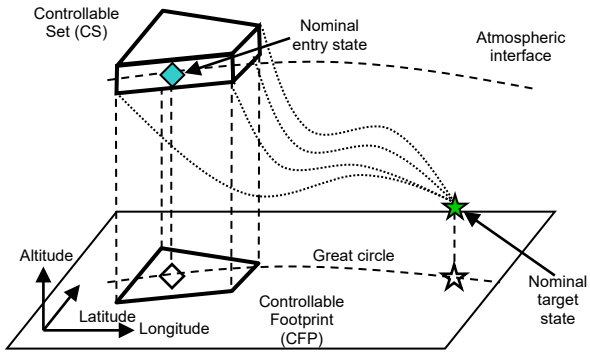

Fig. 2 Controllable set and controllable footprint

Computing the complete reachable and controllable sets or even just their boundaries would be computationally intensive. Instead, we compute certain extremal points in the sets that are of most interest. Extreme values of quantities are displayed for the reachable and controllable longitude-latitude pairs. We use a scoring function that summarizes all the trajectory characteristics to identify preferred areas within the reachable and controllable sets for placing the nominal landing and entry states, respectively.

To illustrate the computation and use of these sets, we obtain the RS and CS for a representative Mars entry mission. Certain future Mars missions are pushing entry, descent, and landing (EDL) technology to accommodate more accurate, higher elevation landings [7]. To date, Mars landings have been at sites with below -1.4 km MOLA (Mars Orbiter Laser Altimeter) elevation. To reach much of the Ancient Highlands, the majority of the southern hemisphere, landing at +2 km MOLA elevations is required. The Mars Science Laboratory (MSL) mission is scheduled to land in the southern hemisphere at +1.6 km MOLA elevation. All previous missions to Mars have had unguided entries with landing errors only guaranteed to be on the order of 100 km. MSL will have a guided entry and is designed to land within 10 km of the desired site. High elevation landing sites are especially challenging because the parachute deployment altitude has to be higher also. Although there exist nominal trajectories that meet the requirements, if they involve lofting in the final entry phase, the amount of lift available to compensate for off-nominal conditions may be less than needed. Some algorithms have been developed [8-9] to provide reference trajectories that preserve control authority to correct for errors during the final entry phase. An alternative vehicle configuration for this type of mission is an ellipsled configuration, which has a higher lift-to-drag (L/D) compared to that of a capsule. The RS and CS for Mars entry will be characterized for these two vehicle configurations to assess the impact of L/D on the entry capability with regard to parachute deployment altitude, landing footprint, feasibility in the entry targeting, and heat rate and load.

II. Entry Problem Formulation

A. Equations of Motion

The equations of motion of an entry vehicle defined with respect to a planet-fixed coordinate frame are [3]

$$
\begin{aligned}
\dot{r} &= V \sin\gamma \\
\dot{\theta} &= \frac{V}{r}\frac{\cos\gamma\cos\psi}{\cos\phi} \\
\dot{\phi} &= \frac{V}{r}\cos\gamma\sin\psi \\
\dot{V} &= -D - g\sin\gamma \\
\dot{\gamma} &= \frac{1}{V}\left[L\cos\sigma - \left(g - \frac{V^2}{r}\right)\cos\gamma\right] + C_\gamma \\
\dot{\psi} &= -\frac{1}{V\cos\gamma}\left(L\sin\sigma + \frac{V^2}{r}\cos^2\gamma\cos\psi\tan\phi\right) + C_\psi
\end{aligned}
\tag{1}
$$

where θ is the longitude, ϕ is the latitude, r is the distance from the center of the planet to the vehicle center of mass, ψ is the heading angle with $\psi = 0$ as due east and $\psi = 90\text{ deg}$ as due north, V is the velocity and γ is the flight path angle. The bank angle is σ, the angle the lift vector is rotated around the velocity axis, with $\sigma = 0$ corresponding to vertical upward and positive σ generating a right turn. L and D are the lift and drag accelerations, defined by

$$
\begin{aligned}
L &= \frac{1}{2}\rho V^2 \frac{S}{m} C_L \\
D &= \frac{1}{2}\rho V^2 \frac{S}{m} C_D
\end{aligned}
\tag{2}
$$

The drag and lift coefficients C_D and C_L are solely functions of the Mach number. Angle of attack is not considered a controllable variable; it takes a Mach number dependent trim value dictated by the vehicle's aerodynamics. S is the reference area, m is the vehicle mass, and ρ is the atmospheric density. g is the gravitational acceleration. The terms C_ψ and C_γ are the Coriolis acceleration components due to planet rotation and can be approximated by

$$
\begin{aligned}
C_\gamma &= 2\omega_p \cos\psi\cos\phi \\
C_\psi &= 2\omega_p\left(\tan\gamma\sin\psi\cos\phi - \sin\phi\right)
\end{aligned}
\tag{3}
$$

where ω_p is the planet angular rotation rate.

B. Downrange, Crossrange and Control Authority Definitions

Distances traveled on the surface of the planet are measured with respect to the great circle arc that includes the projection of nominal entry and target points on the surface of the planet (see Fig. 3). The traveled distance parallel to the great circle arc is the downrange, and the perpendicular distance traveled is the crossrange. Positive crossranges correspond to positions on the starboard side of the great circle arc and negative crossranges correspond to positions on the port side.

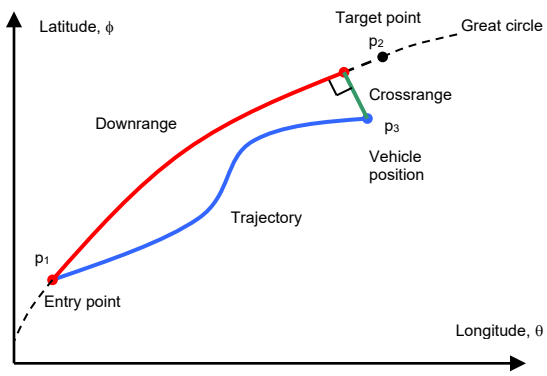

Fig. 3 Trajectory metrics

It is of special interest to deploy the parachute at high altitudes, which is challenging due to the decreased atmospheric density. The altitude acceleration is

$$\ddot{h} = -g - D\sin\gamma + \frac{V^2}{r}\cos^2\gamma + L\cos\gamma\cos\sigma + V\cos\gamma\, C_\gamma \tag{4}$$

The vehicle flight path is controlled by rotating the lift vector around the velocity vector by an angle σ from the vertical, called the bank angle. We refer to the term $L\cos\gamma$ as the altitude control authority (see Ref. [10] for a related definition). Especially close to the deployment point when the velocity is low, it is important to have as much altitude control authority as possible. $L\cos\gamma$ can be increased in different ways, although they all effectively limit lofting motion near the end of entry, because lofting decreases both L and $\cos\gamma$. Further consideration of this issue will be found in Sections IV and V.

C. Vehicle Model

The geometry of an MSL-type capsule [11], inherited from the Viking program, is a double-cone, with an aeroshell forebody shape of a 70 deg sphere-cone. This configuration can provide a lift-to-drag ratio (L/D) of about 0.25. An alternative configuration is the ellipsled vehicle [10-11]. The ellipsled geometry is formed by a spheroid extending into a cylinder, an elliptically blunted cylinder. This configuration can provide an L/D as high as 0.4. Figure 4 shows the MSL and ellipsled configurations.

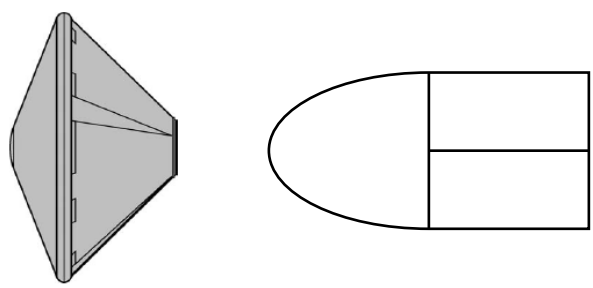

Fig. 4 MSL and ellipsled configurations

The constraints described in the remainder of this subsection apply to both vehicle configurations. Bank angle, the means of flight path control, is limited to $|\sigma| \le 120\ \text{deg}$. Due to limitations in the reaction control system, the bank rate and bank accelerations are limited to $|\dot{\sigma}| \le 20\ \text{deg}/s$ and $|\ddot{\sigma}| \le 5\ \text{deg}/s^2$. The vehicle has constraints on acceleration, dynamic pressure, heat rate and heat load. These constraints will not be imposed in our computation, but the values of those variables will be examined. Convective heat rate ($\dot{Q}$) can be approximated at the stagnation point by the Sutton-Graves equation [12]

$$\dot{Q} = k_q \left(\frac{\rho}{r_n} \right)^N V^M \tag{5}$$

where N=0.5, M=3, $k_q = 1.9027e-4$, ρ is the atmospheric density and r_n is the nose radius of the capsule. The total heat load Q absorbed at the stagnation point the vehicle is the time integral of the heat rate. Dynamic pressure ($\bar{q}$) is given by

$$\bar{q} = \frac{1}{2}\rho V^2 \tag{6}$$

For the results in this paper the lift and drag coefficients are assumed to be constant, a standard approximation for the hypersonic regime. The parameters of the vehicles used in the simulations are shown in Table 1.

Table 1 Vehicle parameters

	MSL-type	Ellipsled	Units
C_D	1.45	1.92	-
C_L	0.36	0.62	-
L/D	0.248	0.323	-
m	2804	2804	kg
S	15.9	15.9	m^2
r_n	0.66	0.66	m

D. Atmospheric and Planetary Models

The atmospheric density ρ is approximated by the exponential function

$$\rho = \rho_0 \exp(-h/h_s) \tag{7}$$

where ρ_0 is the density on the surface of the planet, h is the altitude and h_s is the scale-height. The planet is assumed to be spherical with a surface radius r_p, and hence $h = r - r_p$. Given that in this paper the aerodynamic coefficients are assumed constant, the speed of sound is only needed for the definition of the parachute constraints. For the range of low altitudes involved, the speed of sound can be modeled by a constant velocity V_s. The gravitational acceleration is modeled by $g = \mu / r^2$, where μ is the planet gravitational constant. The numerical values of the planet parameters used in this paper for Mars are shown in Table 2.

Table 2 Martian parameters

Parameter	Value	Units
r_p	3.3866e6	m
μ	4.284e13	m^3/s^2
ρ_0	0.0158	kg/m^3
h_s	9354.5	m
V_s	220	m/s
ω_p	7.095e-5	rad/s

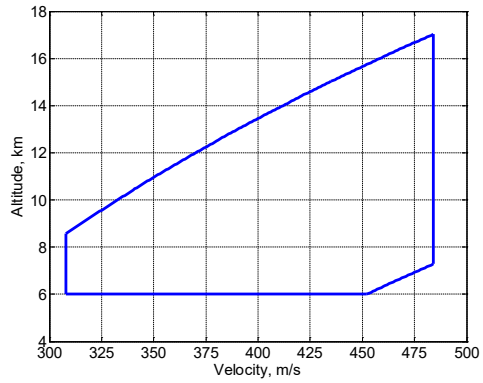

Fig. 5 Disk-Gap-Band parachute box

E. Parachute Deployment Constraints

To date the parachute technology used for Mars entry is that inherited from the Viking program [7]. The selected parachute configuration is the Disk-Gap-Band, which must be deployed in the dynamic pressure range of 300-850 Pa and the Mach number range of 1.4-2.2. The minimum deployment altitude is set to 6 km. When converted to altitude-velocity constraints, for a given atmospheric model, the parachute box, or set of all allowable deployment altitude-velocity pairs, is defined as shown in Fig. 5.

III. Reachable and Controllable Set Definitions

In this section we define a number of sets that are used to characterize the fight capability of an entry vehicle. These sets include feasible, reachable, and controllable sets. Reachable and controllable sets are concepts from systems theory, see for example Ref. [1]. The standard definitions are modified as needed for the entry guidance context. In preparation for defining the reachable and controllable sets, several other sets are first defined. We use standard set notation $S = \{p \in A : property\}$, read "the set S is composed of all points p found in set A such that the property is satisfied". The 'colon' denotes 'such that'.

A. Basic Set Definition

As introduced in Eq. (1), we use the state representation $x = [r, \theta, \phi, V, \gamma, \psi]^T$. We assume that x will take values in a set $\mathrm{X} \subset \Re^6$; X will be specified for the computations, but is left general here. The set $U(t)$ of admissible σ control profiles is defined by

$$U(t) = \left\{ \sigma[0,t] \in C^2[0,t] : |\sigma(\tau)| \le \sigma_{\max}, |\dot{\sigma}(\tau)| \le \dot{\sigma}_{\max}, |\ddot{\sigma}(\tau)| \le \ddot{\sigma}_{\max}, \forall \tau \in [0,t] \right\} \tag{8}$$

where the bank angle profile for the time-interval 0 to t is denoted by $\sigma[0,t]$ and $C^2[0,t]$ denotes the set of continuous functions with continuous first and second derivatives on the interval $[0,t]$. $U(t)$ depends on the time duration t and the constant bounds $\sigma_{\max}$, $\dot{\sigma}_{\max}$ and $\ddot{\sigma}_{\max}$.

The solution to the equations of motion, Eq. (1), at time t for the initial condition $x(0) = x_0$ is expressed by the nonlinear transition map

$$x(t) \equiv \mathrm{T}[t, x_0; \sigma[0,t]] \tag{9}$$

denoting the dependence of $x(t)$ on the elapsed time t, x_0 and the bank angle profile. Because the dynamics are time independent, the initial time is always taken to be zero, without loss of generality. The transition map also depends on the particular force models employed, but because we are not investigating the impact of modeling errors in this paper, our notation does not explicitly indicate the model dependence. The state trajectory for time interval $[0,t]$ is expressed by

$$x[0,t] \equiv \bigcup_{0 \le \tau \le t} \mathrm{T}[\tau, x_0; \sigma[0,\tau]] \tag{10}$$

Thus $x(t)$ is the value of x at time t, whereas $x[0,t]$ is the trajectory segment for the given time interval, a slight abuse of notation.

Let $P \subset \mathrm{X}$ denote the set of states that do not violate the path constraints, defined by

$$P = \{ x \in \mathrm{X} : p(x) \leq 0 \} \tag{11}$$

where $p(x)$ is a vector that can include components specifying the limits on heat rate, acceleration and dynamic pressure, for instance. The deployment set $\Delta \subset \mathrm{X}$, the set of acceptable parachute deployment states is defined by

$$\Delta = \{ x \in \mathrm{X} : d(x) \leq 0 \} \tag{12}$$

where $d(x)$ is a vector specifying the inequality deployment constraints. The definition of $d(x)$ would, for example, include the limits shown in Fig. 5 on the deployment Mach number, dynamic pressure and altitude. If we are focusing our attention on a particular (θ, ϕ) pair, then we further restrict the deployment state to $\Delta|_{(\theta,\phi)} = \{ x \in X : x \in \Delta \text{ and } \Pi(x) = [\theta, \phi]^T \}$, where $\Pi(x) = Cx$ is the mapping that extracts the longitude and latitude state variables from the state vector x, with $C = \begin{bmatrix} 0 & 1 & 0 & 0 & 0 & 0 \\ 0 & 0 & 1 & 0 & 0 & 0 \end{bmatrix}$.

We limit the initial entry states to a subset $X_0 \subset X$ which may restrict the initial values of certain state variables. For instance, traditionally the entry altitude is fixed at $h_0 = 120\ km$; we should have $\gamma_0 < 0$; and the range of initial speeds and heading angles to be considered may be specified, since these values are dictated by the approach trajectory and associated errors. For the reachable set, X_0 will have a single entry state.

Given an initial state $x_0 \in X_0$, $(\sigma[0, t_f], x[0, t_f])$ is a feasible control-trajectory pair with final time $t_f > 0$, if it satisfies the conditions:

- $\sigma[0, t_f] \in U(t_f)$
- $x(t) = \mathrm{T}[t, x_0; \sigma[0,t]] \in P, \quad \forall t \in [0, t_f]$
- $x(t_f) \in \Delta$

Let $F(X_0, X_f)$ denote the set of all feasible control-trajectory pairs with initial state in X_0 and final state in X_f, where X_f is Δ or the more restrictive $\Delta|_{(\theta,\phi)}$ depending on the situation.

B. Reachable Set

The reachable set $RS(x_0) \subset \Delta$ is the set of deployment states with corresponding feasible control-trajectory pairs with entry state x_0; that is

$$RS(x_0) = \{x_f \in \Delta : \exists\ t_f \text{ and } (\sigma[0,t_f], x[0,t_f]) \in F(\{x_0\},\Delta) \text{ with } x(t_f) = x_f\} \tag{13}$$

The symbol $\exists$ denotes 'there exists'. In words, each final state in $RS(x_0)$ can be reached by a feasible control-trajectory pair from x_0 for some t_f, where t_f may be different for each final state. The reachable footprint (RFP) is derived from the $RS(x_0)$ as follows

$$RFP(x_0) = \left\{ [\theta,\phi]^T : \exists\, x_f \in RS(x_0)\ \ with\ \ \Pi(x_f) = [\theta,\phi]^T \right\} \tag{14}$$

Thus to each value of $[\theta,\phi]^T \in RFP(x_0)$, there corresponds at least one value of $x_f \in RS(x_0)$.

C. Optimal Reachable Subset

There is typically more than one feasible control-trajectory pair that leads to a given $[\theta_f, \phi_f]^T \in RFP(x_0)$, i.e., the set $F(\{x_0\}, \Delta|_{(\theta_f,\phi_f)})$ typically has more than one element. Rather than compute all the control-trajectory pairs that lead to a given (θ_f, ϕ_f), it is prudent to first decide which are of most interest and compute only those. Determining extremal points in *F* and *RS* is a means of characterizing these sets.

Using a cost function of the form

$$J(\sigma[0,t_f], x[0,t_f]) = f_0(x(0)) + f_F(x(t_f)) + \int_0^{tf} f_L(x(\tau),\sigma(\tau))\, d\tau \tag{15}$$

with Mayer terms, $f_0(x(0))$ and $f_F(x(t_f))$, and Lagrange term f_L, we determine trajectories that minimize J for each longitude-latitude pair (θ,ϕ) in $RFP(x_0)$ over the set $F(\{x_0\},\Delta|_{(\theta,\phi)})$, and obtain optimal subsets of $F(\{x_0\},\Delta)$ and $RS(x_0)$ that are denoted by $F^J(\{x_0\},\Delta)$ and $RS^J(x_0)$ and defined as

$$F^J(\{x_0\},\Delta) = \bigcup_{[\theta,\phi]^T \in RFP(x_0)} F^J(\{x_0\},\Delta|_{(\theta,\phi)}) \tag{16}$$

where

$$F^J(\{x_0\},\Delta|_{(\theta,\phi)}) = \left\{ \left(\sigma[0,t_f],\, x[0,t_f]\right) \in F(\{x_0\},\Delta|_{(\theta,\phi)}) : J\left(\sigma[0,t_f],\, x[0,t_f]\right) \text{is min over } F(\{x_0\},\Delta|_{(\theta,\phi)}) \right\} \tag{17}$$

and

$$RS^J(x_0) = \left\{ x_f \in RS(x_0) : \exists\ t_f \text{ and } \left(\sigma[0,t_f],\, x[0,t_f]\right) \in F^J(\{x_0\},\Delta) \ \ with\ \ x(t_f) = x_f \right\} \tag{18}$$

Note that the minimization in Eq. (17) is with a free final time.

At a boundary point (θ,ϕ) of $RFP(x_0)$, $F(\{x_0\},\Delta|_{(\theta,\phi)})$ will typically have only one control-trajectory pair, but by default, it minimizes J over $F(\{x_0\},\Delta|_{(\theta,\phi)})$. Though we do not offer a formal proof, it is clear that $RFP^J(x_0) = \left\{ [\theta,\phi]^T : \exists\ x_f \in RS^J(x_0) : \Pi(x_f) = [\theta,\phi]^T \right\}$ is equivalent to $RFP(x_0)$.

D. Controllable Set

The controllable set $CS(\theta_f,\phi_f) \subseteq X_0$ is the set of entry states from which there exists a feasible trajectory to the longitude-latitude pair (θ_f,ϕ_f), and it is given by

$$CS(\theta_f,\phi_f)=\left\{x_0\in X_0:\exists\ t_f \text{ and } \left(\sigma[0,t_f],\, x[0,t_f]\right)\in F\left(\mathrm{X}_0,\Delta|_{(\theta_f,\phi_f)}\right) \text{ with } x(0)=x_0\right\} \tag{19}$$

The controllable footprint (CFP) is derived from the $CS(\theta_f,\phi_f)$ as follows

$$CFP(\theta_f,\phi_f)=\left\{[\theta_0,\phi_0]^T:\exists\, x_0\in CS(\theta_f,\phi_f)\ \textit{with}\ \Pi(x_0)=[\theta_0,\phi_0]^T\right\} \tag{20}$$

For each value of $[\theta_0,\phi_0]^T\in CFP(\theta_f,\phi_f)$, there corresponds at least one value of $x_0\in CS(\theta_f,\phi_f)$. Note that this is a footprint (area on the (θ,ϕ) plane) of feasible entry points, not a landing footprint.

E. Optimal Controllable Subset

Analogous to the reachable set case, there is typically more than one feasible control-trajectory pair for a given $[\theta_0,\phi_0]^T\in CFP(\theta_f,\phi_f)$, i.e., the set $F\left(\mathrm{X}_0|_{(\theta_0,\phi_0)},\Delta|_{(\theta_f,\phi_f)}\right)$ typically has more than one element. We determine trajectories that minimize the cost function J shown in Eq. (15) for each longitude-latitude pair in $CFP(\theta_f,\phi_f)$ and obtain optimal subsets of $F\left(\mathrm{X}_0,\Delta|_{(\theta_f,\phi_f)}\right)$ and $CS(\theta_f,\phi_f)$ denoted by $F^J\left(\mathrm{X}_0,\Delta|_{(\theta_f,\phi_f)}\right)$ and $CS^J(\theta_f,\phi_f)$ and defined as

$$F^J\left(\mathrm{X}_0,\Delta|_{(\theta_f,\phi_f)}\right)=\bigcup_{[\theta_0,\phi_0]^T\in CFP(\theta_f,\phi_f)}F^J\left(\mathrm{X}_0|_{(\theta_0,\phi_0)},\Delta|_{(\theta_f,\phi_f)}\right) \tag{21}$$

where

$$\begin{aligned}F^J\left(\mathrm{X}_0|_{(\theta_0,\phi_0)},\Delta|_{(\theta_f,\phi_f)}\right)=\Big\{&\left(\sigma[0,t_f],\, x[0,t_f]\right)\in F\left(\mathrm{X}_0|_{(\theta_0,\phi_0)},\Delta|_{(\theta_f,\phi_f)}\right)\ \textit{with}\\ &J\left(\sigma[0,t_f],\, x[0,t_f]\right)\ \text{min over } F\left(\mathrm{X}_0|_{(\theta_0,\phi_0)},\Delta|_{(\theta_f,\phi_f)}\right)\Big\}\end{aligned} \tag{22}$$

and

$$CS^J(\theta_f,\phi_f)=\left\{x_0 \in CS(\theta_f,\phi_f): \exists\ \left(\sigma[0,t_f],\, x[0,t_f]\right) \in F^J\left(\mathrm{X}_0, \Delta\,|_{(\theta_f,\phi_f)}\right) \text{ with } x(0)=x_0\ \right\} \tag{23}$$

where the minimization in Eq. (22) is with free final time. We claim that $CFP^J(\theta_f,\phi_f)=\left\{[\theta,\phi]^T : \exists\, x \in CS^J(\theta_f,\phi_f)\ \textit{with}\ \Pi(x)=[\theta,\phi]^T\right\}$ is equivalent to $CFP(\theta_f,\phi_f)$.

IV. Reachable Set Computation and Applications

The trajectories presented in this and the next section have been obtained using the Graphical Environment for Simulation and Optimization (GESOP) [13], a trajectory optimization program that provides several optimization methods. We used the optimization method CAMTOS [14], which includes two discretization options: direct multiple shooting and direct collocation. A two-step strategy was used: direct collocation to obtain the initial guess for direct multiple shooting.

A. Computational Approach

The optimal reachable subset, $RS^J(x_0)$, is computed to study the trajectories with maximum deployment altitude and control authority. The $RFP(x_0)$ is obtained from the optimal reachable subset. The optimal trajectories that form $RS^J(x_0)$ are computed using GESOP after defining the boundary, control and path constraints and the performance index J. The final time t_f is free.

The entry state x_0 is shown in Table 3. Since the initial state is fixed, $X_0=\{x_0\}$. Table 3 also shows the minimum and maximum values of the state variables allowed during entry, defining the set X. No limits on heat rate, dynamic pressure and acceleration are imposed, and hence P equals X. The control constraints that define $U(t)$ are specified in Section II.C. Figure 5 shows the parachute deployment constraints which define the set Δ.

Table 3 Entry state x_0

State Variable	Initial Value	Min. Value	Max. Value	Units
r	3522.2	r_p	3522.2	km
θ	-74.73192	-180	180	deg
ϕ	-43.7513	-90	90	deg
V	5433.5	0	5500	m/s
γ	-15.76793	-45	$\gamma_{\max}$	deg
ψ	15.634524	-90	90	deg

Table 4 Optimization parameters

Variable	Value	Units
k_γ	3.0e5	$1/rad$
k_h	1.0	$1/m$
γ_f	0.0	rad
$\gamma_{\max}$	0.0	rad

The trajectories are optimized to have high control authority and high deployment altitude by minimizing the cost function

$$J = k_\gamma \left[\gamma_f - \gamma\left(t_f\right)\right]^2 - k_h h\left(t_f\right) \tag{24}$$

where the positive constants k_y and k_h are the weighting factors. For the two vehicles, the parameters used in the optimization are shown in Table 4. Limiting the maximum value of γ to an appropriately chosen upper bound $\gamma_{\max}$ is an effective way of limiting the lofting motion and increasing the control authority [8]. In Ref. [9] a term is included in the cost function to bring to zero the deployment flight path angle, which decreases the lofting motion. In practice the vehicle control authority is never high enough to have a positive deployment flight path angle. This term works better than including the Lagrange term $f_L = L\cos\gamma$ in the cost function (see Eq. (15)), which can provide undesirable results since lift is maximized when the altitude is minimized.

B. Application to an MSL-Type Nominal Entry

The nominal RFP is shown in Fig. 6, with contours showing the deployment altitude. Note that nominal implies nominal entry state and nominal vehicle and planet models. The RFP is 175 km long in downrange and 90 km wide in crossrange. Figure 7 presents the deployment velocity profiles. The value of the deployment velocity in the inside of the level sets is the maximum allowed, Mach 2.2 or 484 m/s. Figure 6 shows that near the boundary of the footprint the deployment altitudes are lowest. When all the control authority is used to minimize or maximize downrange, there is none left to raise deployment altitude. The interior of the RFP has the higher deployment altitudes, with the highest at downranges between 620 and 640 km. $RS^J\left(x_0\right)$, as shown in Fig. 7, has a high deployment velocity uniformly in the interior of the set; this maximizes the control authority. All the deployment points are placed at the right edge of the parachute box (Fig. 5).

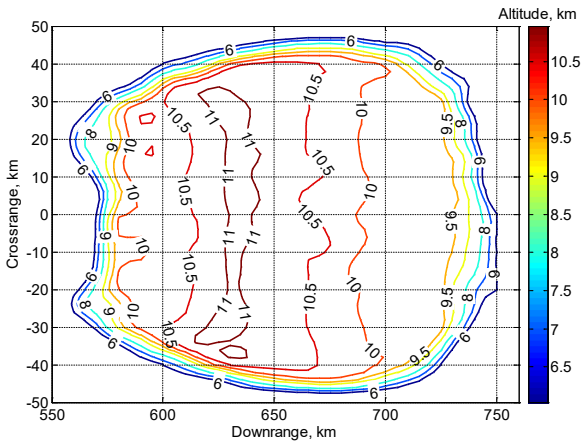

Fig. 6 Nominal RFP and deployment altitudes

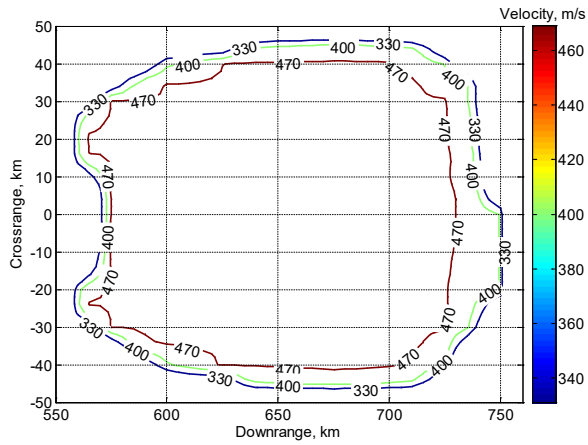

Fig. 7 RFP with deployment velocities

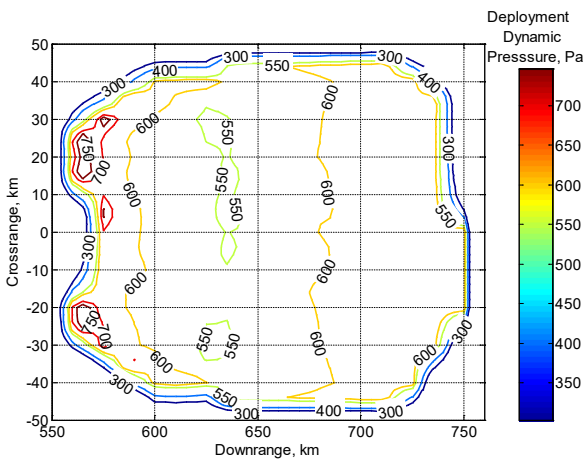

Fig. 8 Deployment dynamic pressure

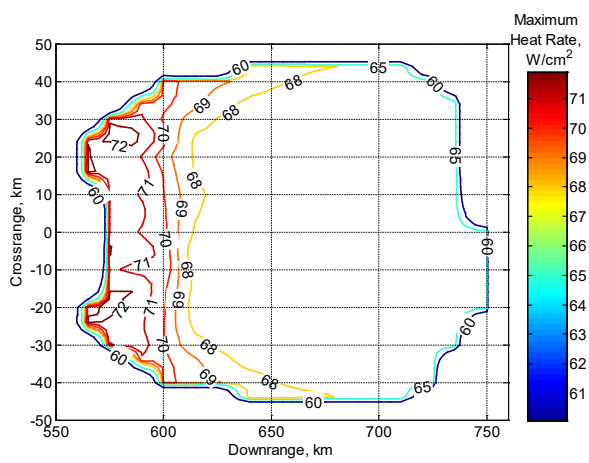

Fig. 9 Maximum heat rate

Figure 8 shows the deployment dynamic pressure. Since the deployment velocity is the same for most of the RFP, the dynamic pressure looks like an inverted version of Fig. 6: low dynamic pressure for high deployment altitude and vice-versa. Figure 9 shows the maximum heat rates achieved during the entry; for the shorter trajectories where the energy has to be dissipated in less time, the maximum heat rates are higher. In general, trajectories with the lowest possible maximum heat rate are desirable to relax the requirements on the thermal protection system (TPS) and to leave margin for off-nominal cases. Figure 10 shows the total heat load. Note that heat load follows a pattern inverse to that of the maximum heat rate.

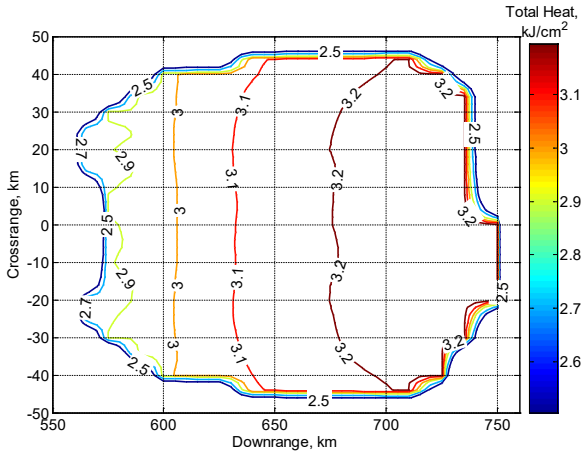

Fig. 10 Total heat load

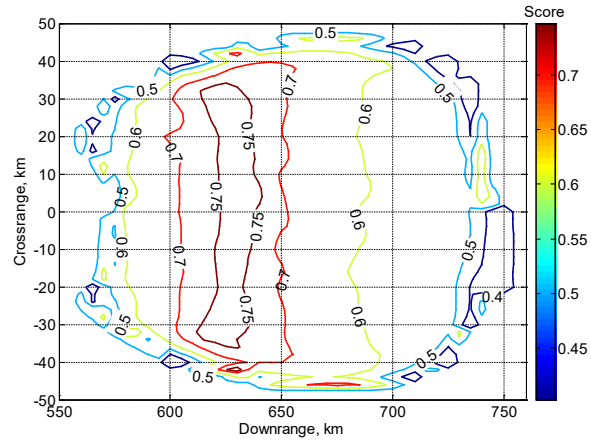

Fig. 11 Score

Table 5 Scoring criteria

Score	Description	Weight	Formula
S_{hf}	Deployment altitude	$W_{hf} = 0.40$	$\dfrac{h(t_f) - h_{\min}}{h_{\max} - h_{\min}}$
S_{dp}	Deployment dynamic pressure	$W_{dp} = 0.00$	$1 - \dfrac{\lvert \bar{q}(t_f) - \bar{q}_0 \rvert}{\bar{q}_{\max} - \bar{q}_0}$
S_{hr}	Maximum heat rate	$W_{hr} = 0.30$	$\dfrac{\dot{Q}_{\max} - (\dot{Q}_{\max})_{\max}}{(\dot{Q}_{\max})_{\min} - (\dot{Q}_{\max})_{\max}}$
S_{hl}	Total heat load	$W_{hl} = 0.30$	$\dfrac{Q - Q_{\max}}{Q_{\min} - Q_{\max}}$

All the points in the $RFP(x_0)$ are, by definition, reachable from x_0. If a point had to be chosen within the RFP to be the nominal deployment target it can be inferred from Figs. 6-10 that the preferred area where the target should be placed near the center of the RFP, where the maximum deployment altitude is the highest and the maximum heat rate and heat load are low. In order to quantitatively evaluate the best target point, one can define a scoring criterion. As an example, we define a scoring function inspired by the approach in Ref. [15], based on the four criteria in Table 5. $h_{\min}$ and $h_{\max}$ are the minimum and maximum deployment altitudes found in RS^J; S_{hf} is 1 if $h(t_f) = h_{\max}$ and 0 if $h(t_f) = h_{\min}$. Deployment conditions in the center of the parachute box are desirable in order to have margins for trajectory tracking errors and to be able to trigger the parachute deployment when the vehicle is

over the target latitude and longitude. S_{dp} is maximum for deployment dynamic pressure equal to $\overline{q}_0$, the midpoint between $\overline{q}_{\min}$ and $\overline{q}_{\max}$; i.e. $\overline{q}_0 = 0.5(\overline{q}_{\max} + \overline{q}_{\min})$. W_{dp} is set to 0 in for the scoring of RS^J since it interferes with S_{hf}; however it will be used for the scoring of CS^J. $\dot{Q}_{\max}$ is the maximum heat rate achieved during the trajectory, $(\dot{Q}_{\max})_{\max}$ and $(\dot{Q}_{\max})_{\min}$ are the maximum and minimum $\dot{Q}_{\max}$ found in the trajectories that form RS^J; hence S_{hr} is 1 when $\dot{Q}_{\max} = (\dot{Q}_{\max})_{\min}$ and 0 when $\dot{Q}_{\max} = (\dot{Q}_{\max})_{\max}$. Q is the total heat load, and S_{hl} is 1 when Q equals the minimum heat rate found in the trajectories that form RS^J and 0 when it equals the maximum. With these definitions, the score S is computed adding up all the scores multiplied by the corresponding weight, as shown in Eq. (25). With these definitions the score S is a number between 0 and 1 provided that the weights add up to 1. The score for the nominal MSL mission is shown in Fig. 11. The best area to place the nominal target point is between 600 and 650 km downrange and -20 and +20 km crossrange.

$$S = W_{hf} S_{hf} + W_{dp} S_{dp} + W_{hr} S_{hr} + W_{hl} S_{hl} + W_{bs} S_{bs} \tag{25}$$

C. Application to an Ellipsled-Type Nominal Entry

The nominal RFP for the ellipsled vehicle is shown in Fig. 12 along with the nominal RFP for the MSL vehicle. The ellipsled RFP is 300 km long in downrange and 180 km wide in crossrange, significantly larger that the one achievable with the MSL vehicle. Similar results are presented in Ref. [3], where optimal landing footprints are calculated (under several simplifications) for vehicles with different L/Ds. Figure 13 shows the maximum deployment altitude. Comparing with Fig. 6, the ellipsled vehicle can reach higher deployment altitudes: 15.5 km compared to 11 km for the MSL configuration. Parachute deployment altitudes for different L/Ds are shown in Ref. [7]; the corresponding trajectories exhibit lofting motion.

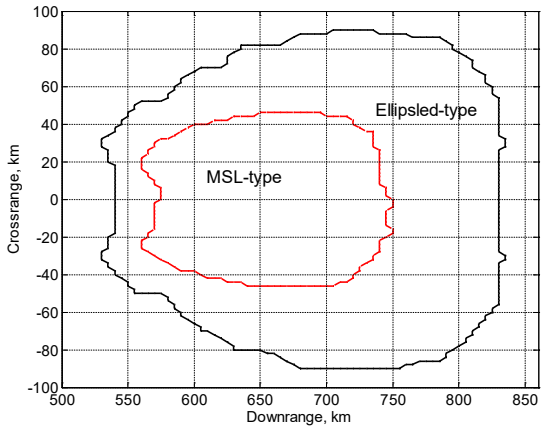

Fig. 12 Ellipsled vs. MSL RFP

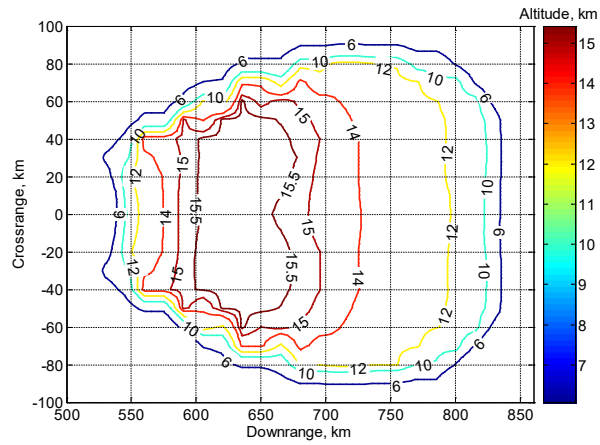

Fig. 13 Deployment altitude

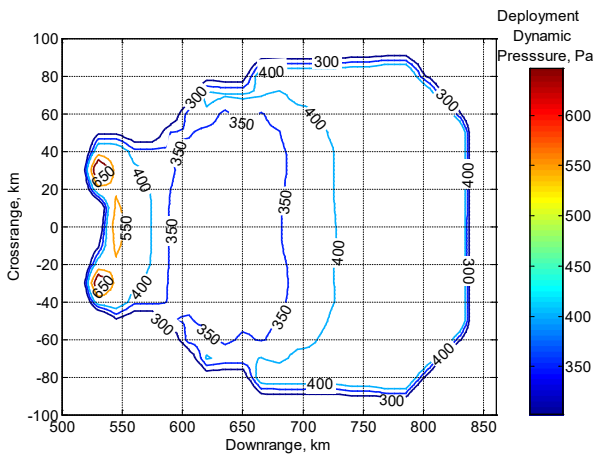

Fig. 14 Deployment dynamic pressure

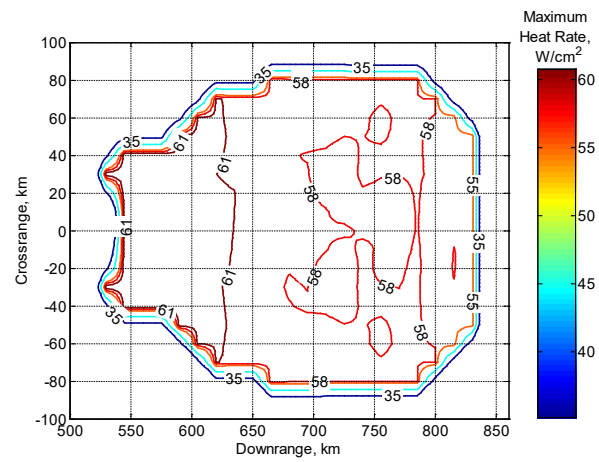

Fig. 15 Maximum heat rate

Figure 14 shows the deployment dynamic pressure. The deployment velocities of the states in RS^J for the ellipsled are the maximum allowed for most of the area of the RFP, as in Fig. 7. Hence, Fig. 14 is the mirror image of Fig. 13. The deployment dynamic pressures are as low as 350 Pa, compared to 550 Pa for the MSL vehicle (Fig. 8). Figure 15 shows the maximum heat rate achieved for each of the trajectories with end states in RS^J. The higher L/D of the ellipsled vehicle generates higher trajectories with lower atmospheric density and thus with lower heat rate (compare to Fig. 9).

Figure 16 shows the total heat load, which is roughly the reverse pattern shown in Fig. 15. Short trajectories have higher heat rate and lower heat load; long trajectories have lower heat rate and higher heat load. As with the

maximum heat rate, the higher trajectories of the ellipsled configuration provide a lower heat load compared to the MSL configuration (see Fig. 10). The scoring function is the same used for the MSL configuration shown in Table 5 and Eq. (25). The score distribution for the ellipsled is shown in Fig. 17.

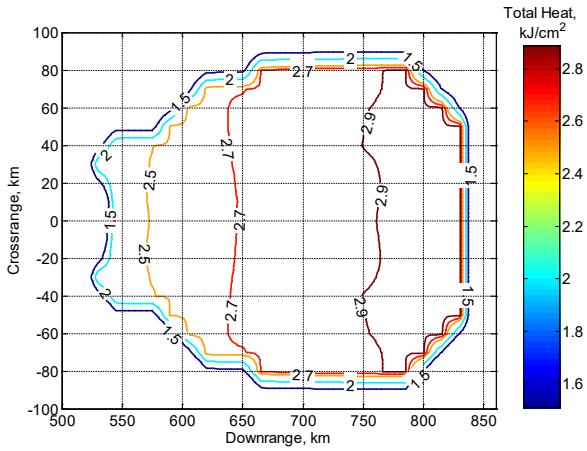

Fig. 16 Total Heat Load

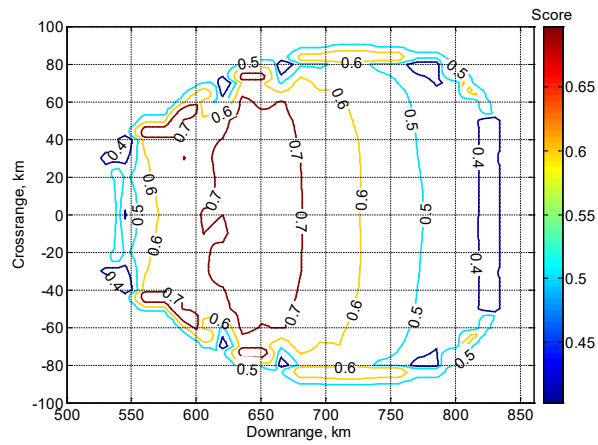

Fig. 17 Score

D. Discussion

Higher L/D provides a larger RFP, which translates into more landing sites reachable from an entry point and more capability to accommodate entry state dispersions. An increase in L/D also allows higher deployment altitude and lower deployment dynamic pressure, maximum heat rate and heat load.

For guidance algorithms like EAGLE [16] that combine a trajectory planner and a trajectory tracker, the reachable sets can be used to analyze the range and optimality of the trajectory planner. Because the boundaries of the RS are achieved by minimizing or maximizing a function of the final state variables, e.g., downrange or crossrange, any planner that is not solving these trajectory optimization problems will only be capable of planning trajectories to an interior subset of the RS. How large this subset is relative to the RS is the measure of the capability of the planning algorithm. Ref. [4] shows a comparison of LFPs obtained with EAGLE and optimal ones.

The RS can be used to decide the best nominal target site for a given entry state and planet and vehicle models. A scoring function based on multiple criteria can identify the best area for the target site. The choice of scoring function and weights affects strongly the result; the scoring function used in this paper is only an illustration. For both vehicles, the scoring maps show that there is an area at around 625 km downrange and 0 km crossrange where the target can be placed for best overall performance for both configurations (compare Figs. 11 and 17).

V. Controllable Set Computation and Applications

A. Computational Approach

Similar to the strategy for the RS, we compute an optimal subset of the controllable set, denoted $CS^J(\theta_f, \phi_f)$ and the associated footprint $CFP(\theta_f, \phi_f)$. We first specify the boundary constraints, the path constraints, the control constraints and the cost function for the optimal control problem. Table 6 shows the entry boundary constraints for both the MSL-type and the ellipsled-type vehicles, which define X_0 in each case. Table 6 also shows the minimum and maximum values of the state variables allowed during entry, which define X in each case. These limits are never reached except for the one corresponding to maximum flight path angle, which is constrained to a specified $\gamma_{\max}$ to ensure the vehicle has enough control authority by avoiding a lofting motion, as explained in Section II.A . No constraints on dynamic pressure, heat rate, heat load and total acceleration are imposed, and hence $P = X$. The values of these variables will however be examined. For all the trajectories, $\gamma_{\max} = 0$ deg . The deployment set Δ is defined in Fig. 5. The control constraints that define $U(t)$ are specified in Section II.C. The target pair (θ_f, ϕ_f) is set to $(\theta_f, \phi_f) = (-61.08\,, -40.0)$.

Table 6 Entry state and state constraints

State variable	Nominal entry value	Minimum value	Maximum value	Units
r	3522.2	r_p	3522.2	km
θ	Free	-180	180	deg
ϕ	Free	-90	90	deg
V	5433.5	5800	0	m/s
γ	Free	-45	$\gamma_{\max}$	deg
ψ	ψ_0	-90	90	deg

The variations in the initial heading angle ψ_0 are assumed to be caused by a deorbit timing error, and are thus associated with a lateral offset from the nominal entry point. The initial heading angle ψ_0 of each trajectory in CS^J matches the heading angle of a point on the nominal great circle containing the nominal entry point and the target site (θ_f, ϕ_f) used in the previous section and specified in Table 3. The particular point on the nominal great circle is the one whose perpendicular contains the perturbed entry point as shown in Fig. 18. The initial radius is consistent

with the standard 120 km altitude. The initial velocity is fixed since for typical entry state dispersions its variation from a nominal value is small. This assumption is not necessary; the initial velocity can be varied at the expense of more computation.

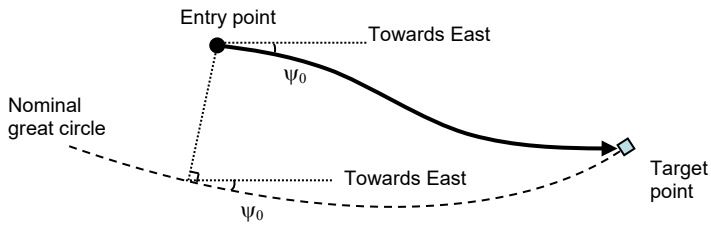

Fig. 18 Initial heading angle

We will view the 6-dimensional *CS* by projecting it along the other coordinate axes onto the (θ,ϕ) plane; this is the *CFP*. Then we show the level sets for quantities of particular interest. For example, a more comprehensive characterization of the entry corridor [2] is achieved by computing for each point $(\theta_0,\phi_0)\in CFP$, the trajectories with the maximum and minimum flight path angles. Thus the cost function is

$$J = k\gamma(0) \tag{26}$$

where k is 1 for minimum entry flight path angle, and -1 for maximum entry flight path angle. No term for increasing the control authority is included in the cost function, because it would compete with the maximizing the entry flight path angle, since steep entries present higher control authority. Instead, the path constraint $\gamma < \gamma_{\max}$ is imposed.

B. Application to an MSL-Type Entry

Continuing with the characterization of an MSL mission, CS^J is presented in this section. Figure 19 shows the CFP for the minimum entry flight path angle case, which has a size of 1200 km in downrange and an average of around 200 km in crossrange. An entry point at a downrange of 1200 km and a crossrange of 100 km means that

from this entry point a vehicle has to fly 1200 km parallel to the nominal great circle and 100 km normal to it. The CFP is not symmetric due to the Coriolis effects. Figure 20 shows the CFP with the maximum entry flight path angles. The nominal entry point used in the previous section (Table 3) corresponds to a downrange of 640 km and a crossrange of 0 km.

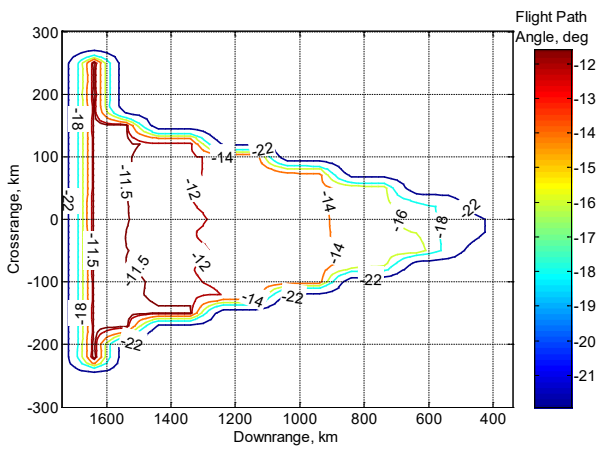

Fig. 19 CFP for minimum entry flight path angle

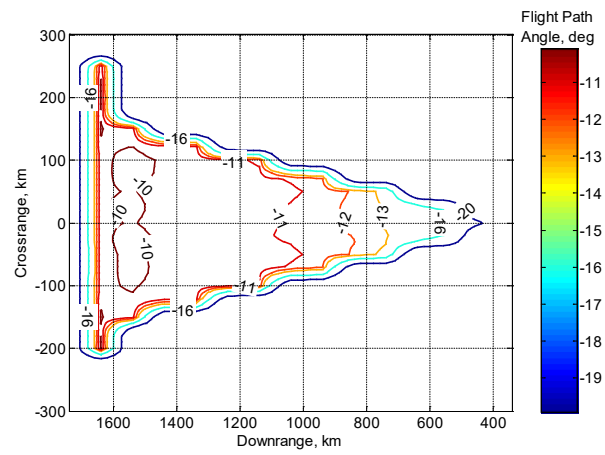

Fig. 20 CFP for maximum flight path angle

Shorter downranges require steeper entry flight path angles, and longer downranges require shallower entry flight path angles. Figure 21 shows the difference between the maximum and minimum entry flight path angles, i.e., the depth of the CS^J, terminology used in Refs. [2, 5, 6]. The depth decreases on the edges of CS^J. Figure 22 shows the contours of maximum heat rate on the CFP for the steepest entry flight path angle case, and Fig. 23 shows the total heat load for the case of shallowest entry flight path angle. Restricting our attention to values of heat rate and heat load at the maximum and minimum entry flight path angle values is based on the assumption that the extremal values of those quantities occur there. In Ref. [17], approximate formulas for lifting entry with constant $\sigma = 0$ show that the maximum heat rate increases as the entry angle steepens and that the total heat load increases as the entry angle becomes shallower. Our assumption is that in a controlled entry (non-constant σ) these tendencies are still valid. Figure 22 shows that the maximum heat rate is increasing for steeper entry flight path angles and lower downranges. If the maximum heat rate is limited to a certain value, due to TPS limits, the minimum entry flight path angle and the minimum downrange would be constrained.

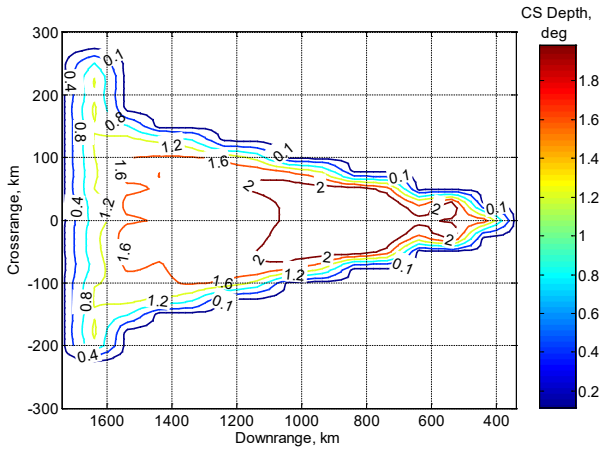

Fig. 21 Entry flight path angle depth

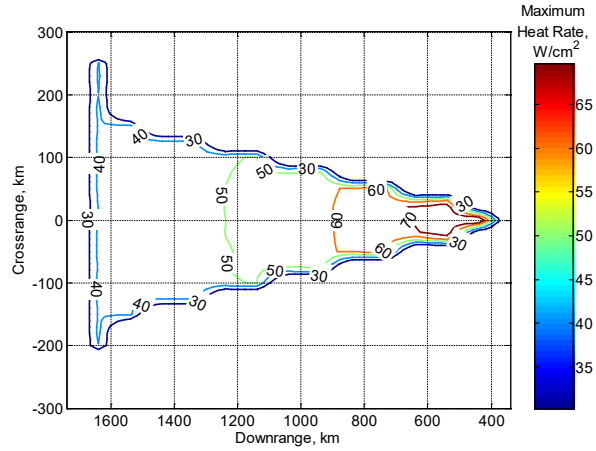

Fig. 22 Maximum heat rate (minimum $\gamma(0)$ case)

Figure 23 shows the total heat load for the maximum entry flight path angle case, in which the heat loads are higher than for the minimum flight path angle case. The pattern is the reverse of the one for maximum heat rate: heat load is maximum where heat rate is minimum and vice-versa. Limits in the TPS mass fraction, which determines the maximum heat load allowed, constrain the maximum entry flight path angle and maximum downrange.

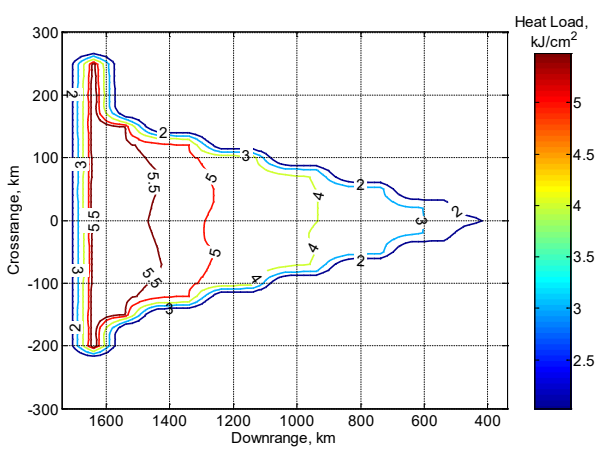

Fig. 23 Heat load (maximum $\gamma(0)$ case)

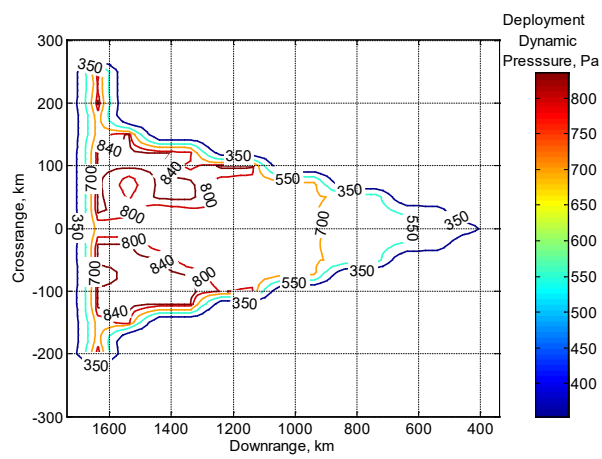

Fig. 24 Deployment dynamic pressure (minimum $\gamma(0)$ case)

Figs. 24 and 25 show the deployment dynamic pressure for the minimum and maximum entry flight path angle cases, respectively. The deployment altitude for all the trajectories is very close to the minimum 6 km (this allows

for the optimization of the entry flight path angle), and hence the deployment dynamic pressure is an indication of the deployment velocity. Trajectories with shallow entry flight path angle have a higher deployment velocity and dynamic pressure than trajectories with steep entry flight path angles.

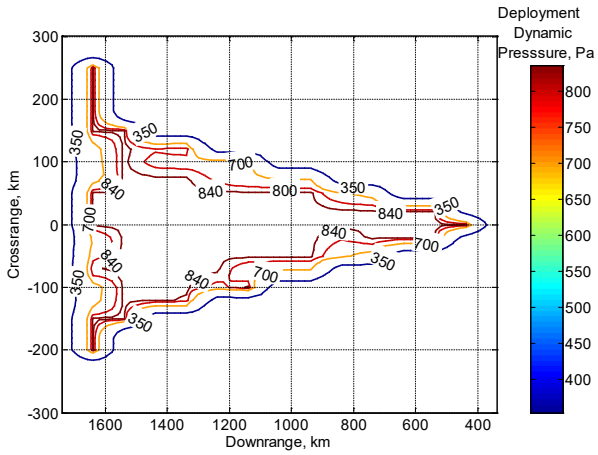

Fig. 25 Deployment dynamic pressure (maximum $\gamma(0)$ case)

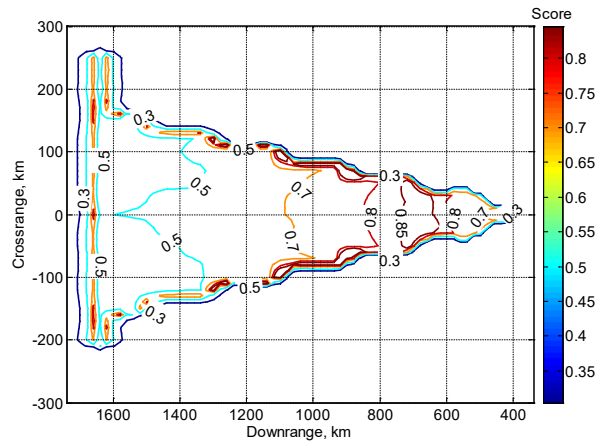

Fig. 26 Score (minimum $\gamma(0)$ case)

The scoring function used for the CS is the one used for the RS (Eq. (25)), with $W_{hf} = 0$, $W_{hr} = 0.333$, $W_{hl} = 0.333$, and $W_{dp} = 0.333$. Figs. 26 and 27 show the score map for the minimum and maximum entry flight path angle cases. The scores are higher for steeper entry flight path angles at a given entry point. Figure 28 shows the entry maximum and minimum entry flight path angles along the line of zero crossrange with the score level sets, which have been linearly interpolated between the two surfaces. The best places to set the entry point would be between 600 and 800 km downrange and as close to the steepest allowable entry flight path angle as possible. Of course if modeling errors and the need for control margin and approach navigation accuracy are taken into account, the steepest entry angle would not be chosen.

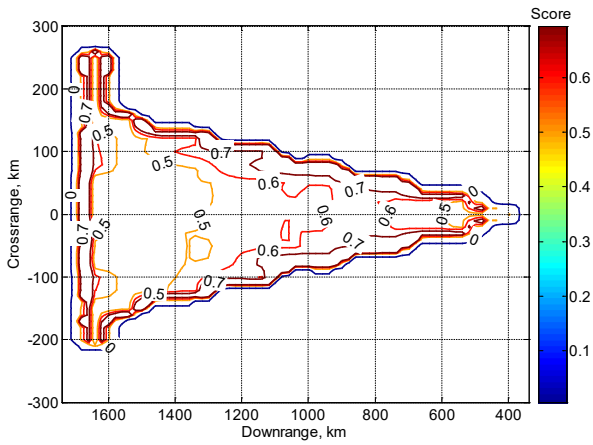

Fig. 27 Score (maximum $\gamma(0)$ case)

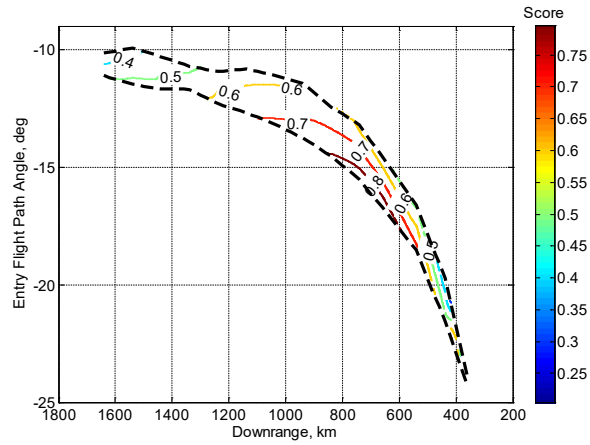

Fig. 28 Score (zero crossrange)

C. Application to an Ellipsled-Type Vehicle

The CFPs for the MSL-type and the ellipsled vehicles are compared in Fig. 29. The increase L/D of the ellipsled allows mainly for more crossrange. The dimensions of the ellipsled CFP are 1300 km in downrange, and around 300 km in crossrange on average. For the ellipsled, Fig. 30 shows the minimum flight path angle, and Fig. 31 the maximum flight path angle.

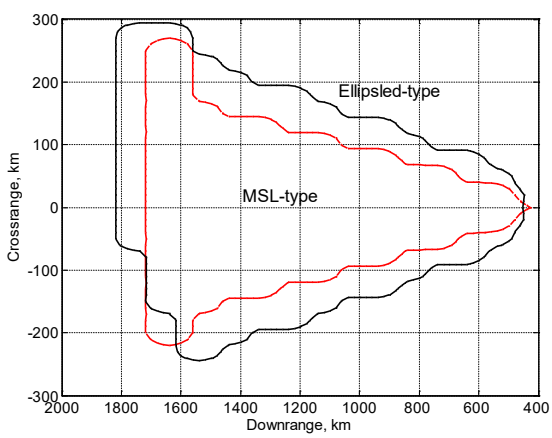

Fig. 29 CFP MSL vs Ellipsled

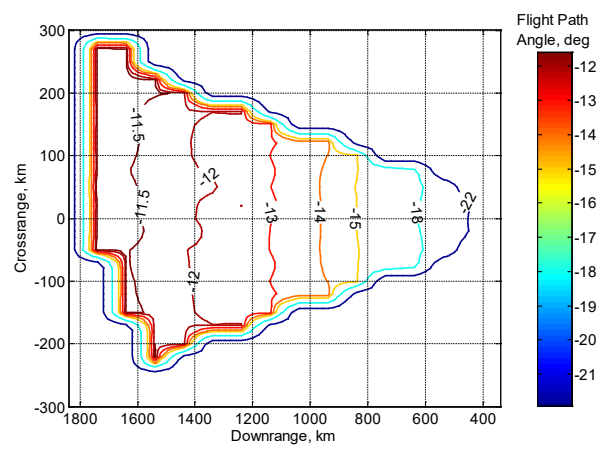

Fig. 30 CFP for minimum entry flight path angle

Compared to the MSL-type vehicle, the ellipsled can accommodate a wider range of entry flight path angles for trajectories with the same downrange. This can be seen in Fig. 32: a 4 degree variation in flight path angle can be

accommodated by the ellipsled. MSL-type vehicles can accommodate a variation of 2 degrees. See Fig. 40 for a comparison of the flight path angle depth between both vehicles along the zero crossrange line.

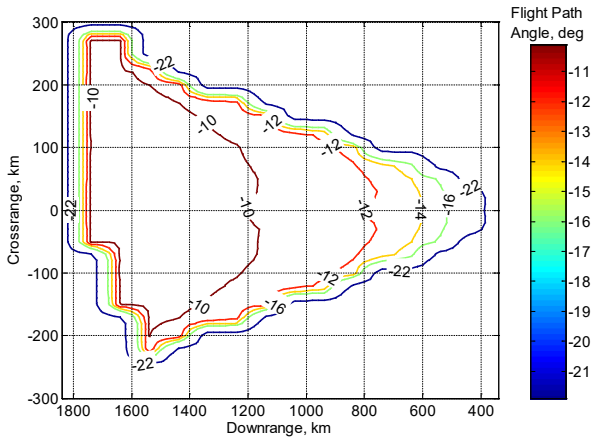

Fig. 31 CFP for maximum entry flight path angle

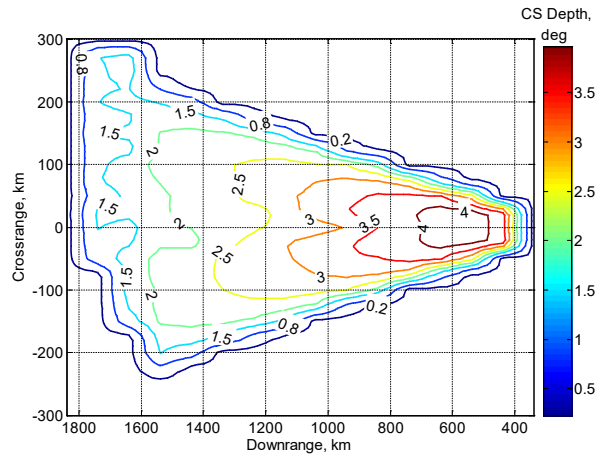

Fig. 32 Entry flight path angle depth

The higher altitude trajectories of the ellipsled vehicle have lower heat rates and heat loads than trajectories flown by the MSL-type vehicle for the same downranges. Maximum heat rate is depicted in Fig. 33; heat load is shown in Fig. 34. Figures 35 and 36 show the deployment dynamic pressure. As with the MSL-type vehicle, the deployment altitude is very close to the minimum allowed, so dynamic pressure is indicative of the deployment velocity. The deployment dynamic pressure is higher for shallower entry flight path angles.

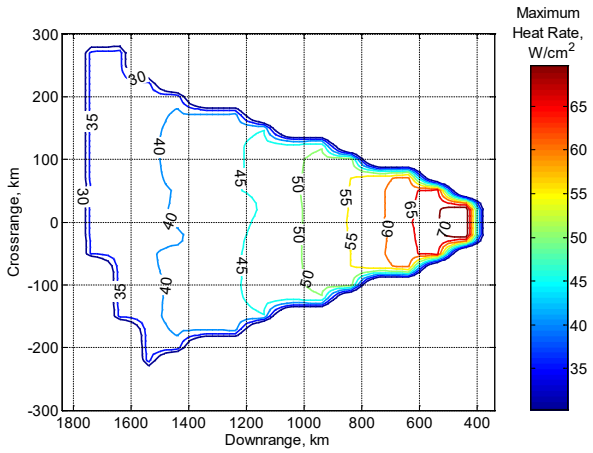

Fig. 33 Maximum heat rate (minimum $\gamma(0)$ case)

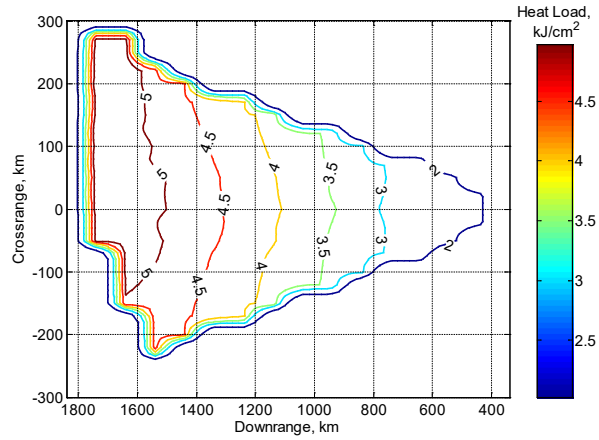

Fig. 34 Heat load (maximum $\gamma(0)$ case)

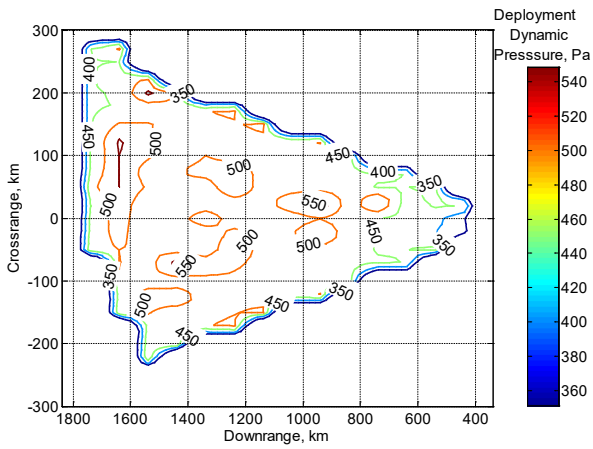

Fig. 35 Dynamic pressure (minimum $\gamma(0)$ case)

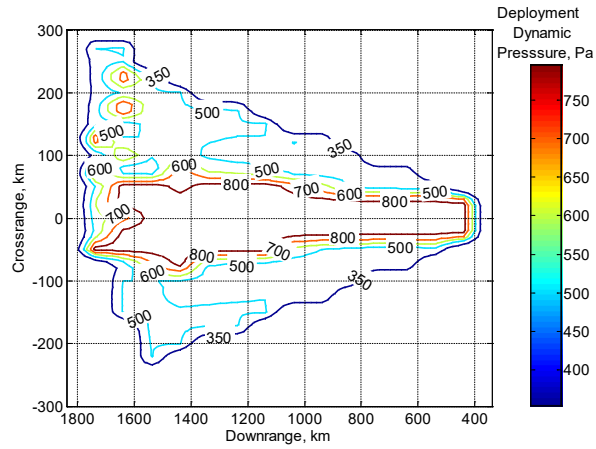

Fig. 36 Dynamic pressure (maximum $\gamma(0)$ case)

Scoring maps are calculated with the same weights used for the MSL vehicle. The score is higher for steeper entry flight path angles, as seen in Figs. 37 and 38. Maximum and minimum entry flight path angle along the zero crossrange line and the level set of the scores are shown in Fig. 39. It can be seen that the best area to place the entry state, for zero crossrange, is between 800 and 1400 km and the lowest possible entry flight path angle.

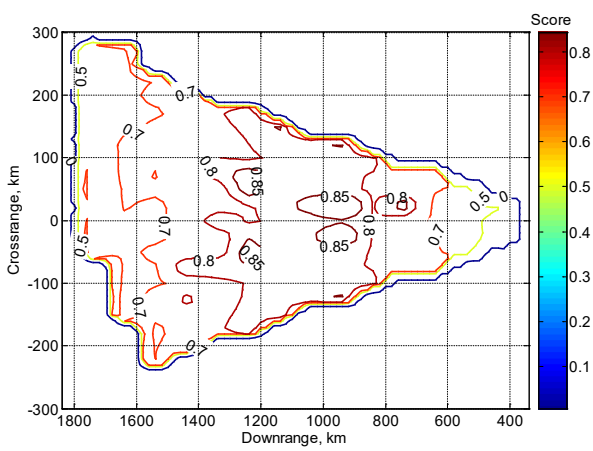

Fig. 37 Score (minimum $\gamma(0)$ case)

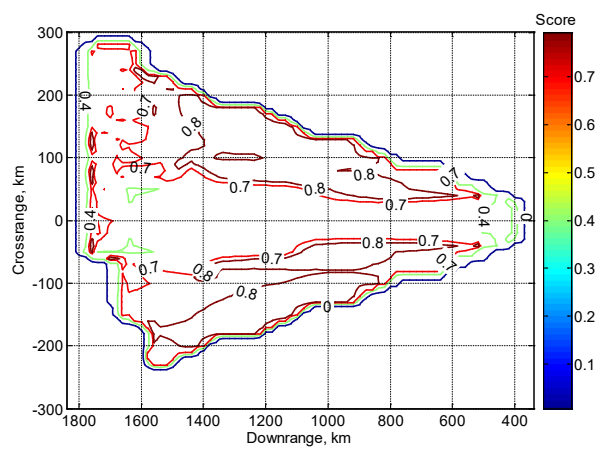

Fig. 38 Score (maximum $\gamma(0)$ case)

Figure 40 presents a comparison between the acceptable entry flight path angles along the zero crossrange line, showing that the vehicle with higher L/D can accommodate a wider range of entry flight path angles. A direct relation between L/D and entry flight path angle depth is also shown in Ref. [6].

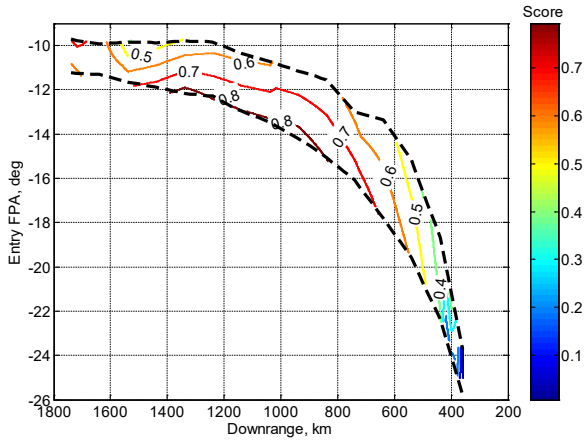

Fig. 39 Score (zero crossrange)

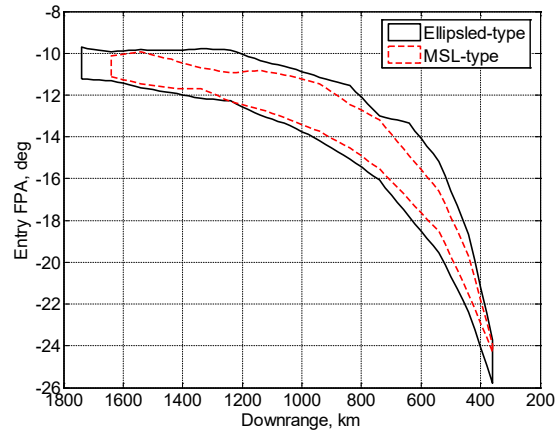

Fig. 40 Entry flight path angle depth comparison (zero crossrange)

D. Discussion

Figures 29 and 40 show that an increase in L/D enlarges the CS, thus there are more feasible entry states for a given deployment location; it especially allows for a wider range of entry flight path angles. Note that the freedom in the entry flight path angle diminishes the differences in size between the CFPs of the MSL-vehicle and the ellipsled-vehicle, as opposed to the RFP, where the differences were significant (see Fig. 12).

The CS can be used to evaluate a trajectory planner. The set of entry states from which a planner can construct a trajectory to a designated landing site can be compared to the CS to evaluate the capability of the planner. The evaluation of the planner will depend on the design objectives. In some cases it is desirable for the planner to cover as much of the CS as possible so that large entry state dispersions can be accommodated. In other cases, covering the CS is not important; for example, planning trajectories with high control authority and high deployment altitude may be most important even at the expense of reduced coverage.

The CS^J can be used, via the computation of a scoring function to select a nominal entry state. The scoring function and weights used in this paper are only an illustration of the utility of the computation of this set for mission planning and analysis. The approach navigation accuracy should also be compared to the CS size for the selection of the nominal entry state; it is desirable that the uncertainty of the nominal entry state 'fits' in the CS. This also highlights the utility of the CS to link the entry phase to previous phases.

VI. Conclusions

As means of characterizing the envelope of feasible entry trajectories for a given vehicle, we have defined reachable and controllable sets and the related reachable and controllable footprints. The sets were used to characterize the Mars entry problem for two vehicle configurations with special attention to high altitude parachute deployment and high control authority trajectories. We discussed how these sets can be used to evaluate entry guidance algorithms and how they can be used to select a nominal entry state and a nominal parachute deployment site.

The results obtained in this paper required extensive computation. The computation of these sets in this manner is feasible for pre-mission design, but for operational use, a faster approach would likely be required.

Although the examples in this paper were limited to Mars entry, reachable and controllable set analysis is applicable to entry at Earth and other atmosphere-bearing planets and satellites. For example, the new crew exploration vehicle, Orion, will be required to deliver the crew safely to a designated landing site with high accuracy, without violating crew and vehicle constraints, from a large range of different entry conditions [18]. In the case of a return from the Moon, accommodating trajectories with downranges from 3100 to 5400 nm will require skip-entry trajectories. The controllable set to a designated landing site can be used to evaluate the capability of an entry algorithm to meet the downrange requirements. Entry from low earth orbit (from the International Space Station for instance) will require handling abort and emergency scenarios as autonomously as possible, for which the computation of the reachable set can be used to select the landing site from among all those reachable from the vehicle's entry position.

Acknowledgments

The research reported in this paper was sponsored by the Jet Propulsion Laboratory, California Institute of Technology under contract with the National Aeronautics and Space Administration.

References

[1] Sontag, E.D., "Mathematical Control Theory," 2nd ed., Springer, New York, 1998.

[2] Wingrove, R.C., "A Study Of Guidance To Reference Trajectories For Lifting Reentry At Supercircular Velocity," NASA TR-R-151, Ames Research Center, Moffet Field, CA, December 1963.

[3] Vinh, N. X., "Optimal Trajectories in Atmospheric Flight," Elsevier, New York, 1981.

[4] Saraf, A., Leavitt, J. A, Ferch, M., and Mease, K. D., "Landing Footprint Computation for Entry Vehicles," AIAA Paper 2004-4774, August 2004.

[5] AviDyne, K. et al., "Guidance and Navigation for Entry Vehicles," NASA-SP-8015, November 1968.

[6] Wong, T. J., and Slye, R. E., "The Effect of Lift on Entry Corridor Depth and Guidance Requirements for the Return Lunar Flight," NASA TR-R-80, Ames Research Center, Moffett Field, CA, 1961.

[7] Braun, R.D. and Manning, R. M., "Mars Exploration Entry, Descent, and Landing Challenges," J. Spacecraft and Rockets, Vol. 44, No. 2, pp. 310–323, 2007.

[8] Benito, J. and Mease, K., "Entry Trajectory Planning For Higher Elevation Landing," AAS Paper 07-309, AAS/AIAA Astrodynamics Specialist Conference, Mackinac Island, MI, August 2007.

[9] Boada, J., Benito, J. and Mease, K., "Near Optimal Planner for Higher Elevation Landing," 2008 Pegasus-AIAA Student Conference, Prague, Czech Republic.

[10] GESOP - Graphical Environment for Simulation and Optimization, Ver. 4.7.0, Astos Solutions, Germany, http://www.astos.de/.

[11] Masciarelli, J. P., Westhelle, C. H. and Graves, C. A., "Aerocapture Guidance Performance for the Neptune Orbiter," AIAA Paper 2004-4954, AIAA Atmospheric Flight Mechanics Conference, August 2004, Providence, RI.

[12] Lockwood, M. K., Sutton, K., Prabhu, R., and Powell, R. W., "Entry Configurations and Performance Comparisons for the Mars Smart Lander," AIAA Paper 2002-4407, AIAA Atmospheric Flight Mechanics Conference, Monterey, CA, August 2002.

[13] Sutton, K., and Graves, R., "A General Stagnation-Point Convective-Heating Equation for Arbitrary Gas Mixtures," NASA TR R-376, 1971.

[14] Gath, P. F., "CAMTOS - A Software Suite Combining Direct and Indirect Trajectory Optimization Methods," Ph.D. thesis, University of Stuttgart, Nov. 2002.

[15] Hanson, J. and Jones, R., "Test Results for Entry Guidance Methods for Space Vehicles," Journal of Guidance, Control, and Dynamics, Vol. 27, No. 6, 2004, pp. 960-966.

[16] Saraf, A., Leavitt, J. A., Chen, D. T., and Mease, K. D., "Design and Evaluation of an Acceleration Guidance Algorithm for Entry," Journal of Spacecraft and Rockets, Vol. 41, No. 6, 2004, pp. 986–996.

[17] Loh, W. H. T.,"Re-entry and Planetary Entry Physics and Technology," Vol. 1, Springer-Verlag, New York, 1968.

[18] Broome, J. and Johnson, W., "Orion Entry, Descent, and Landing Performance and Mission Design," AIAA Paper 2007-6430, AIAA Guidance, Navigation and Control Conference and Exhibit, Hilton Head, SC, August 2007.